Contents lists available at ScienceDirect

Arabian Journal of Chemistry

journal homepage: www.ksu.edu.sa

Original article

Enhancing the pure water splitting using carbon-iron oxide–carbon nitride (Fe_2O_3-C/CN) heterostructure

Muhammad Qasim [a,*], Muhammad A. Younis [b], Fahim A. Qaraah [c], Mohamed A. Ghanem [d,*]

[a] Qilu Institute of Technology, Basic Department, Jinan 250200, China
[b] International Collaborative Laboratory of 2D Materials for Optoelectronics Science and Technology of Ministry of Education, Institute of Microscale Optoelectronics, Shenzhen University, Shenzhen 518060 China
[c] School of Chemical Engineering and Technology, Tianjin University, Tianjin 300350, China
[d] Chemistry Department, College of Science, King Saud University, Riyadh 11451, Saudi Arabia

ARTICLE INFO

Keywords:
Photocatalysis
H_2/O_2 production
Charge transfer
direct Z-scheme photocatalyst
Heterojunction

ABSTRACT

Highly efficient pure photocatalysts for water-splitting applications have long been plagued by structure imperfectness, narrowband light absorption, rapid charge recombination, and sluggish surface reaction kinetics. Herein we report a Z-scheme heterojunction photocatalyst made of Fe_2O_3, CN, and a conductive carbon layer (C) at the interface of the two materials (Fe_2O_3-C/CN). The structure has been characterized using a range of physicochemical and photo-electrochemical techniques. Compared to pristine Fe_2O_3, the Fe_2O_3-C/CN photocatalyst revealed superior photogenerated charge carriers, transport efficiency, and suppressed recombination process along with the conductive carbon layer acting as a mediator. The optimum composite of (5 wt% Fe_2O_3-C/CN) shows excellent activity towards pure water splitting, which reached 408 and 199 μmol/g.h for H_2 and O_2 evolution respectively, and a solar-to-hydrogen conversion efficiency of approximately 0.29 % when used for the pure water splitting process. Such a superior efficiency and production rate offer great potential for pure water splitting, and provide an alternative solution to future green energy production processes.

1. Introduction

The rapid consumption of fossil fuels and rapid growth of the population have brought severe ecological problems and global energy crises. Therefore, an increasing interest in sustainable and clean energy sources has spurred the global transition towards efficient processes for the production of green hydrogen and energy storage systems.(Sun et al., 2023; Wang et al., 2023). The green production of hydrogen fuel offers an optimal long-term sustainable and environmentally friendly energy source.(Yu et al., 2022). However, the current global production of hydrogen through sustainable water electrolysis is only about 7 %, limiting its potential as a clean, economical, and domestically sourced energy supply (Kumar and Lim, 2023). Photo-catalysis and Electro-catalysis are the two primary green methods used for the decomposition of water (Gui et al., 2024; Ji et al., 2024). To make clean hydrogen energy, the key is to develop a cost-effective and efficient semiconductor photocatalyst. Pure water splitting by photocatalysis using semiconductor catalysts has been predicted as the silver bullet toward environmental remediation (Hou et al., 2022; Pang et al., 2023; Qasim et al., 2023). To achieve this goal, it's important to make photocatalysts that can absorb light well, separate charges quickly, have good redox capabilities, and last a long time. Among various photocatalysts, carbon nitride (CN) looks promising for converting solar energy efficiently because it's easy to work with and has the right band alignment, appropriate visible light harvesting bandgap, robust physicochemical stability, high surface area, and nontoxic properties (Gong et al., 2022; Xiao et al., 2023; Xue et al., 2019; Zeng et al., 2023). Unfortunately, the photoactivity of single-component CN is rather dissatisfactory due to low conductivity inherently photo carrier separation, and surface kinetics (Chen et al., 2021; Rao et al., 2023).

Z-scheme photocatalysis is an innovative process that offers several advantages for water splitting and is a crucial component for the development of photocatalysts for renewable energy production. In this scheme, two different semiconductors with suitable band structures are combined to mimic the natural photosynthesis process. The Z-scheme can improve the photocatalytic activity and ultimately higher hydrogen production by optimizing the two semiconductors' specific redox reactions. Moreover, the Z-scheme system can minimize electron-hole

* Corresponding authors.
E-mail addresses: qasim@qlit.edu.cn (M. Qasim), mghanem@ksu.edu.sa (M.A. Ghanem).

https://doi.org/10.1016/j.arabjc.2024.105902
Received 22 May 2024; Accepted 7 July 2024
Available online 11 July 2024

recombination, reduce energy loss, and improve overall quantum efficiency via effective utilization of reducing (H_2 production) and oxidizing (O_2 production) half-reaction (Ayodhya, 2023; Das et al., 2022; Zhao et al., 2021).

Metal-organic framework (MOF) materials have unique performance advantages, such as controllable pore size and modified pore surface, low density, and high surface area, which makes the new porous material widely used in many fields, for example, adsorption, photocatalysis, and catalysis (Ma et al., 2024; Wei et al., 2023a; Zhang et al., 2024a). Within this context of MOFs-driven two-step photo-excitation, an artificially engineered CN-based Z-scheme incorporated semiconductor heterojunctions has been widely reported as an effective photocatalyst for boosting the water-splitting reactions (Du et al., 2023; Zhou et al., 2023; Wei et al., 2023b; Zhang et al., 2022; Zhao et al., 2021; Jiang et al., 2018; Hussein Abdurahman et al., 2023). In contradistinction to attenuated redox functionalities of electron/hole pairs in type-II heterojunction, the Zscheme mechanism ensures the preservation of redox reactivity of photo-carriers, enhances absorption capacity and facilitates charge separation. However, the bottleneck in constructing CN-based Z-schemes shifts to identifying a second semiconductor with matched band alignment (Bi et al., 2023a). Hematite (Fe_2O_3), possessing a bandgap of 2 to 2.2 eV, exceptional resistance to photo-corrosion, lack of toxicity, and high earth abundance, emerges as a promising candidate for integration into CN-based photocatalysts (Qasim et al., 2019). Despite its high recombination limited diffusion length, and more positive conduction band make it conducive to combining with CN, potentially forming a direct Z-scheme heterojunction (Ma et al., 2021). However, the structural mismatch-induced interfacial charge transfer resistance between Fe_2O_3 and CN necessitates a solid-state carrier mediator at the interface to accumulate the photo-charge carriers (Bi et al., 2023b; Ma et al., 2024; Wei et al., 2023b; Zhang et al., 2024a).

We have found and resolved certain deficiencies in the existing literature about the Z-scheme method for photocatalytic pure water splitting, specifically regarding systems based on Fe_2O_3 and CN. Our research addresses these deficiencies by offering a thorough comprehension of the synergistic interactions inside this particular heterostructure and how they might be enhanced for increased efficiency. Our research aims to overcome these shortcomings by providing a comprehensive understanding of the synergistic interactions inside this specific heterostructure and exploring ways to strengthen them for improved efficiency. Our study presents a new method of modifying the Fe_2O_3-C/CN heterostructure along with the conductive carbon layer. This novel technique utilizes the conductive qualities of the carbon layer to improve the separation and transfer efficiency of photo charges in the Fe_2O_3/CN heterostructure, overcoming the limits of prior studies. We utilize sophisticated characterization methods, to gain a more profound understanding of the charge dynamics and interfacial properties of the carbon layer-modified Fe_2O_3/CN heterostructure. This is to understand the mechanism and the function of the carbon layer in the Z-scheme system which is essential for hydrogen fuel production.

Herein, we present the development of a novel solid-state Z-scheme photocatalyst by incorporating amorphous carbon-evolved Fe_2O_3 (Fe_2O_3-C) nanoparticles embedded on CN, aimed at enhancing pure water splitting. The successful formation of this heterojunction is attributed to the simultaneous annealing of an iron-based metal–organic framework (MOF, MIL-235) and a post-synthetic CN substrate. The amorphous carbon layer formed on the Fe_2O_3 surface is derived from the pyrolysis of the MOF (MIL-235) material. Furthermore, the high-temperature calcination induces a solid interface within the composite, particularly forming an amorphous carbon layer around Fe_2O_3 nanoparticles which behaves as an electron shuttle. These parameters synergistically ensure and facilitate carrier flow within the photocatalyst framework. The optimized photocatalyst exhibits remarkable pure water splitting under visible solar irradiation ($\lambda \geq 420$ nm). Importantly, such heterostructures are widely utilized because of their excellent stability in photocatalytic pure water splitting applications. Overall, this study aims to advance the technology of water splitting by developing and utilizing a novel nanostructured material composed of iron oxide, carbon, and carbon nitride arranged in a heterostructure configuration. This innovative approach is intended to significantly boost the efficiency and effectiveness of the water-splitting process, contributing to the development of sustainable hydrogen production methods.

2. Experimental section

2.1. Chemicals and reagents

Ferric tri-chloride hexahydrate ($FeCl_3{\cdot}6H_2O$, 99 %; pure), dicyandiamide (DCDA), N, N-dimethylformamide (DMF), terephthalic acid (H_2BDC), and ethanol anhydrous (C_2H_6O) were purchased from Sinopharm Chemical Reagent Co., Ltd. Na_2SO_4 electrolyte, platinum salt for Pt photo-deposition. In all the experiments, DI water was used. All chemical reagents were of analytical grade and used without any purification.

2.2. Synthesis of Fe_2O_3-C catalyst

Initially, 2.0 g of $FeCl_3{\cdot}6H_2O$ and 100 mg of terephthalic acid (H_2BDC) were added in a solution comprising 20 mL of ethanol and 20 mL of N, N-dimethylformamide (DMF) in an autoclave of total volume 100 mL. A clear solution was obtained after stirring for 20 min, and then sealed in the autoclave and placed in an oven at 120 °C for 6 h. Finally, a dark brown suspension was washed several times with ethanol and DMF to remove the soluble contaminants. Eventually, Fe_2O_3-C was obtained by drying the obtained product at 90 °C for 8 h in a vacuum oven.

2.3. Synthesis of carbon nitride CN and Fe_2O_3-C/CN composite

For the synthesis of CN, typically, DCDA (10.0 g) was dissolved in water at 40 °C, then transferred to an autoclave and put in an oven at 140 °C for 12 h. The obtained sample was washed with DI water many times to eliminate the residuals and heated at 80 °C to dry. Finally, the white powder is placed in a horizontal muffle furnace and heated at 600 °C about 4 h at a heating rate of 5 °C/min and then cooled down naturally to obtain porous carbon nitride (CN).

A simplistic synchronous calcination method was applied to the synthesis of Fe_2O_3-C/CN composite, with MIL-235 acting as the template to synthesize Fe_2O_3 enclosed by an amorphous carbon layer (Fe_2O_3-C). In a typical procedure, 100 mg of synthesized CN and a certain amount of Fe_2O_3-C (1.0, 3.0, 5.0, and 10.0 wt%) were transferred into DI (40. mL) water and sonicated for about half an hour. After that, the solution was filtered and heated at 90 °C to completely evaporate the water. The dried composite was then transferred to a combustion corundum boat with cover and calcinated at 300 °C for about 2 h at a heating rate of 5 °C/min in air.

3. Results and discussion

3.1. Structural and surface area characterizations

Starting from MOF (MIL-235) which serves as an excellent template for the controlled synthesis of Fe_2O_3 nanoparticles. The simulated and synthesized XRD analysis of MIL-235 is shown in Fig. S1. During the synthesis process, the organic ligands of MIL-235 can decompose to form a carbon layer at about 300 °C that coats the Fe_2O_3 nanoparticles. This carbon layer enhances the electrical conductivity and protects the Fe_2O_3 nanoparticles from agglomeration, maintaining their high surface area and active sites. The combination of Fe_2O_3-C nanoparticles and the CN results in a synergistic effect that enhances the photocatalytic performance and improves light absorption, charge transfer, and overall stability of the photocatalytic system. Next, we perform XRD and FTIR analysis of pristine and composite heterostructure.

Fig. 1a shows the X-ray diffraction (XRD) patterns and crystal structure of the obtained pristine Fe_2O_3-C, CN, and Fe_2O_3-C/CN heterostructure photocatalysts. For CN the XRD pattern (red line) shows two characteristic peaks appeared at 12.8° and 27.8° suggesting a pristine nature of CN and corresponding well to the crystal plan of (100), and (002) respectively (Sarkar et al., 2022). The crystal face at (100) represents the repeating unit of tri-s-triazine in its planar structure, whereas the crystal face at (002) appeared from the interlayer stacking of aromatic segments. All the composite photocatalytic materials showed similar diffraction peaks around 27.8° indexed as the (002) crystal plane of CN indicated that the crystal phase of CN is well maintained after incorporation of Fe_2O_3-C catalyst. On the other hand, sharp and obvious peaks were detected for the Fe_2O_3-C/CN composite samples consistent with the standard atlas card (JCPDS 24-0072) suggesting a high crystalline nature was achieved using the solvothermal method. Notably, the peak intensity of CN in Fe_2O_3-C /CN showed a slight opposite trend with increasing the amount of Fe_2O_3-C. This phenomenon can be attributed to the effect of Fe_2O_3-C on the inhibition of CN diffraction, indicating that there is a tight interface between Fe_2O_3-C and CN (Qasim et al., 2021).

The FT-IR spectrum was acquired to further investigate the formation of pristine CN, Fe_2O_3-C, and Fe_2O_3-C/CN heterostructure in a range of 450–4000 cm^{-1} as shown in Fig. 1b. For pristine CN sharp peak is observed around 800–890 cm^{-1} representing the breathing mode of tri-s-triazine units, and the absorption peaks appeared at 1200–1650 cm^{-1} indicating the stretching vibration mode of C-N, and C=N heterocycles. Additionally, broad peaks observed between 3000 and 3500 cm^{-1} suggest the stretching vibration of N–H bonds. The characteristic peaks of pristine CN are also observed in the composite (Fe_2O_3-C/CN) heterostructure representing a well-maintained chemical structure of CN and Fe_2O_3-C. Furthermore, the two intense peaks appeared around 460 and 526 indicating the stretching vibration mode of the Fe-O bond (Qasim et al., 2021).

Next, the nitrogen adsorption–desorption isotherms of the obtained photocatalyst composites were conducted to measure the porosity, diameter, and pore volume (BET-BJH) analysis as shown in Fig. 1c. The composites' adsorption–desorption isotherms show type IV adsorption–desorption isotherm according to IUPAC type classification, which is correlated with a hysteresis cycle suggested the meso and macroporous material architecture (Qasim et al., 2019). Additionally, the plot of pore volume and pore radius derived using the BJH method (Fig. 1d) revealed the pore size distribution within the range from 20 to 100 Å. The average pore size and surface area of pristine CN, Fe_2O_3-C, and optimized (5 wt% Fe_2O_3-C/CN) composite are 1.72/22.96, 1.90/22.37, and 7.40 nm/44.19 m^2 g^{-1}, respectively as shown in supporting information Table S1. These results confirm the presence of mesoporous nanotexture in the photocatalytic composites which is consistence with the SEM and TEM morphology characterizations shown above not only

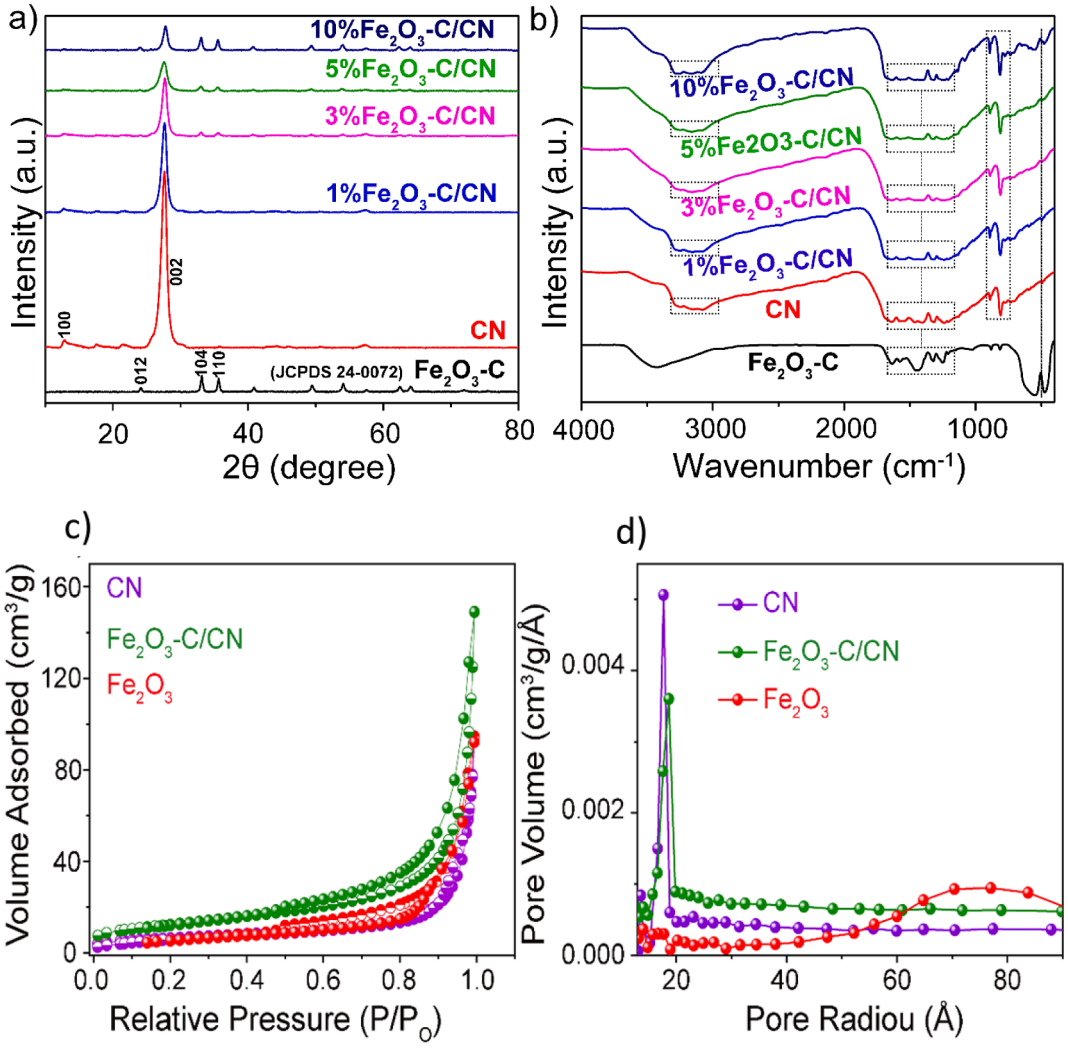

Fig. 1. A) xrd patterns of fe_2O_3-C, CN, and Fe_2O_3-C/CN photocatalyst composites, b) the corresponding FTIR patterns, and c, d) N_2 adsorption–desorption isotherms of pristine CN, Fe_2O_3-C, and their composite, along with corresponding pore size distribution.

enhanced the photocatalytic activity but also enhanced the light absorption and decreased scattering.

3.2. Morphological and compositional analyses

Fig. 2a provided a schematic illustration for the conversion of MOF (MIL-235) into Fe_2O_3-C and formation of (Fe_2O_3-C/CN) heterostructure composites while Fig. 2b shows the microstructure analysis of optimized composite (5 wt% Fe_2O_3-C/CN), where iron oxide (Fe_2O_3-C) nanoparticles (blue circles) are embedded on the surface of pristine carbon nitride nanosheet and free from agglomeration. This understanding can be further verified by magnified HRTEM analysis where the lattice spacing of 0.27 nm can be assigned to the Fe_2O_3 {1 0 4} plane as shown in (Fig. 2c). A closer investigation indicates that the surface of the nanoparticle is covered by a thin carbon layer of thickness about 3–4 nm. Next, (Fig. 2 e-h) shows the energy dispersive X-ray (EDX) mapping analysis of the photocatalyst composite to verify the presence of C, N, Fe, and O elements respectively. The elemental analysis was utilized to determine the composition of C in the Fe_2O_3-C, Fe_2O_3-C/CN heterostructure. Upon meticulous measurement, we have determined that the weight percentage of carbon (C) in the composite material Fe_2O_3-C/CN is greater, specifically 2.15, in comparison to the weight % of carbon (C) in pure Fe_2O_3/CN, which is 1.65. This investigation presents additional proof supporting the presence of a carbon layer on Fe_2O_3. This result further corroborates our prior findings. In addition, (Fig. S2 a, d) shows the SEM images of porous pristine CN structure along with the successful formation of Fe_2O_3-C nanoparticles through the solvothermal route. Similarly, (Fig. S2 b, c) showed that the Fe_2O_3-C nanoparticles are successfully embedded on the surface of CN without any agglomeration. Furthermore, to verify the formation of the carbon layer we perform a mapping analysis of pristine Fe_2O_3-C nanoparticles as shown in Fig. S3.

To determine the atomic valance state of the photocatalyst composites, X-ray photoelectron spectroscopy (XPS) was then performed as depicted in Fig. 3. Fig. 3a, represents the C 1S core XPS spectra of

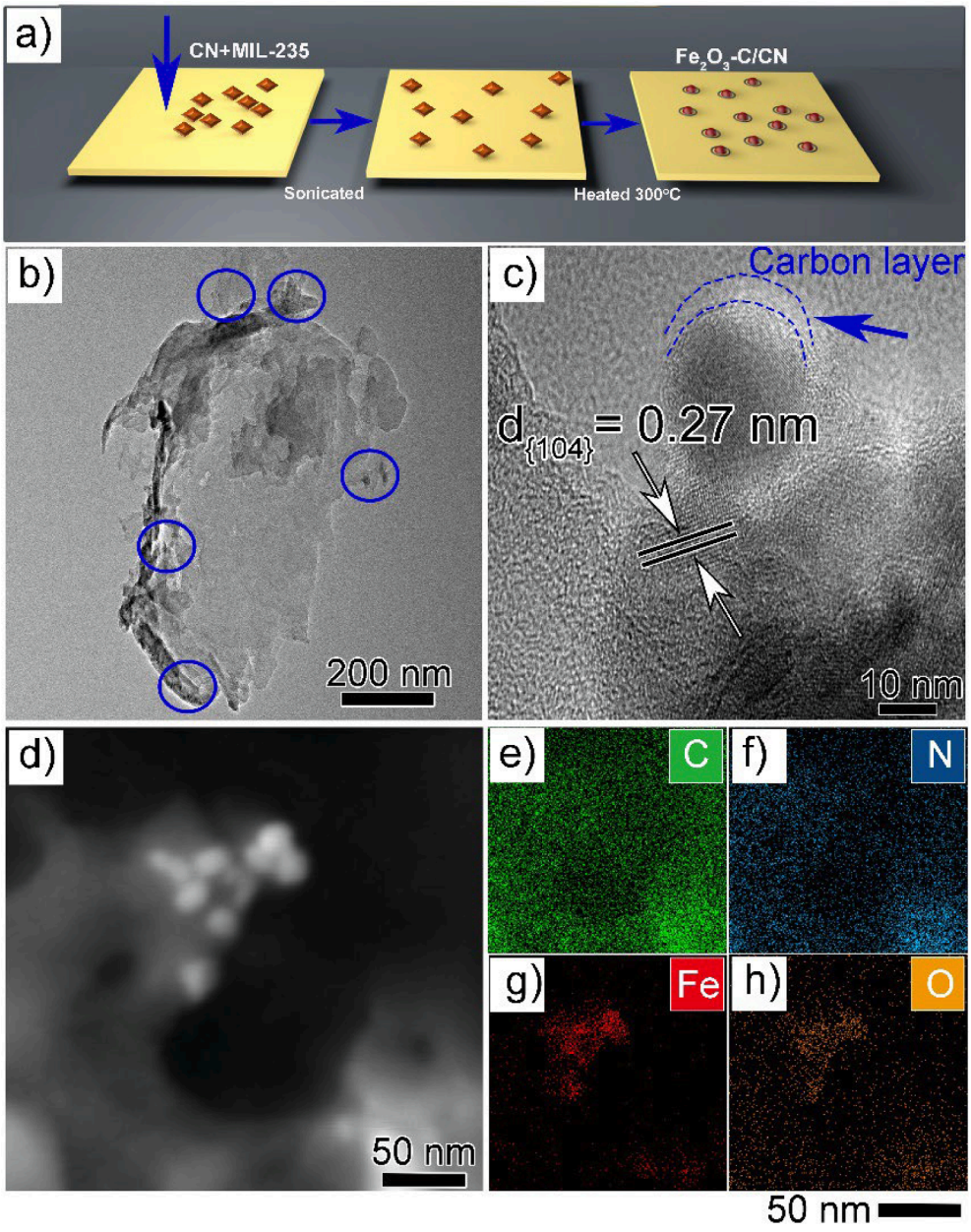

Fig. 2. A) schematic diagram b) tem, c) hrtem images of 5%fe_2O_3-C/CN composite along with carbon layer, d) STEM and e-h) the corresponding mapping images of C, N, O, and Fe, respectively.

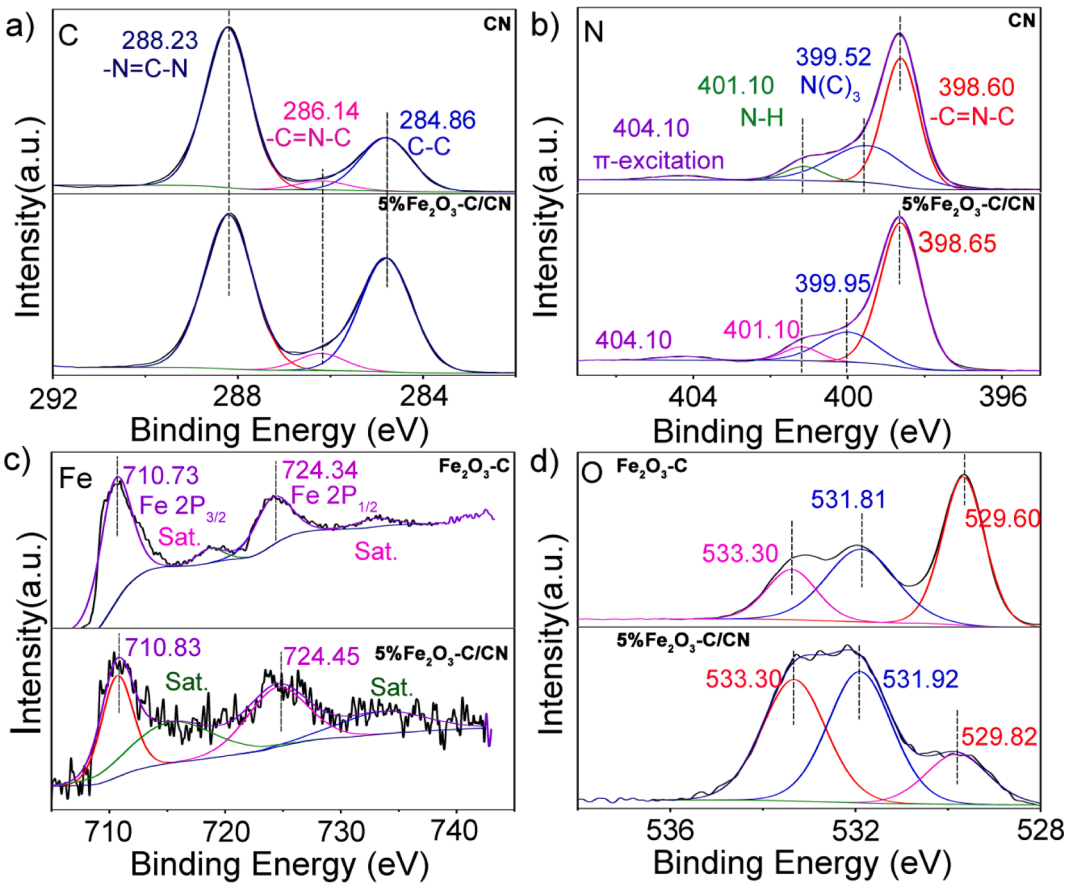

Fig. 3. XPS high-resolution spectra of pristine CN along with 5.0 wt% Fe_2O_3-C/CN samples, a) C 1s, b) N 1s, c) Fe 2p, and d) O core spectra, respectively.

pristine CN, and composite photocatalyst, respectively. It shows three typical binding energy peaks located at 284.86 eV, 286.14 eV, and 288.23 eV, indicated to (C–C), sp^2-C connected to $–NH_2$ (C-NH_2), and sp^2-C bounded to N in aromatic ring (N-C=N), respectively (Iqbal et al., 2023; Ma et al., 2023; Palanivel et al., 2023). Similarly, N 1 s XPS spectra split into four peaks situated at 398.60, 399.52, 401.10, and 404.10 eV, respectively for both pristine CN and 5 wt% Fe_2O_3-C/CN composite. These peaks can be indexed to sp^2-hybridized nitrogen (C-N = C), tertiary nitrogen (N-3C) groups, amino groups (C-N-H), and π-excitation, respectively (Fig. 3b) (Iqbal et al., 2023; Ma et al., 2023; Yavuz and Erten-Ela, 2022). However, a slight peak shift towards higher binding energies was observed in the composite heterostructure as compared to pristine CN suggesting the successful construction of heterojunction with strong interaction between Fe_2O_3-C and CN substrate which increases the charge transfer process at the interfaces (Danish et al., 2022; Vignesh et al., 2022). Usually, peak shifted to higher binding energy indicates a decrease in electron concentration due to modulated interfacial charge transfer attributed to the formation of heterostructure (Qasim et al., 2021). Furthermore, Fe 2p core spectra of pristine Fe_2O_3-C, and 5 wt.%Fe_2O_3-C/CN, composite exhibit characteristic peaks arising at 710.73 eV, 724.34 eV, 710.83 eV, and 724.45 eV respectively, along with two shake-up satellite peaks. Finally, Fig. 3d presents the high-resolution XPS spectra of O 1 s of pristine Fe_2O_3-C, and composite photocatalyst. The spectra exhibit three characteristic peaks two of them located at around 533.30 eV and 531.81 eV corresponding to C=O and C-O, respectively. In addition, the third peak located at 529.60 eV originated from Fe-O-C bonding (Qasim et al., 2023; Vignesh et al., 2022).

3.3. UV–vis, bandgap, and band structure analysis

To understand the electronic and band structure of the composites, Fig. 4a shows the collective UV–vis absorption spectra of pristine CN, and Fe_2O_3-C, and their composites are measured in the wavelength range from 300 to 800 nm. The absorption edges of the composite materials exhibited no discernible alterations when contrasted with pristine g-C_3N_4. However, there is a notable enhancement in the absorption intensity of the composite within the visible light spectrum. This enhancement can be attributed to the inclusion of Fe_2O_3, which possesses a broad and intense absorption of visible light. Essentially, the redshift in the absorption region and the augmentation of absorption serves to facilitate the absorption of more solar energy, leading to a greater number of excited electrons. Consequently, this phenomenon enhances the photocatalytic efficiency. Fig. 4(b, c) shows the corresponding Kubelka-Munk plots of the Fe_2O_3-C and CN respectively, where the band gaps of (Fe_2O_3-C and CN can be estimated to be 2.09 eV and 2.52 eV, respectively. To estimate the conduction band (CB) levels under the dark of Fe_2O_3-C and CN sample, Fig. 4(d, e) shows the Mott-Schottky results performed at a frequency of 1.0 kHz in 0.1 M Na_2SO_4 solution. The flat band potential (E_{fb}) of the semiconductors was represented by the intercept created from an extended line of the Mott-Schottky curve along the x-axis. The results indicated that the E_{fb} of Fe_2O_3-C and CN samples are −0.30 and −1.65 V (vs. Ag/AgCl), corresponding to 0.31 and −1.04 V (vs. RHE), respectively. Generally, the CB value is supposed to be 0.1 to 0.2 eV more negative than that of the E_{fb}. Therefore, the actual values of Fe_2O_3 and CN are 0.11 and −1.24 eV vs. RHE, respectively (Dang et al., 2023). However, the reliability of the VBM was also confirmed through experimental validation employing valence band X-ray photoelectron spectroscopy (VB-XPS) on the manufactured samples (Fig. S4 a, b). The VBM values for Fe_2O_3-C and CN

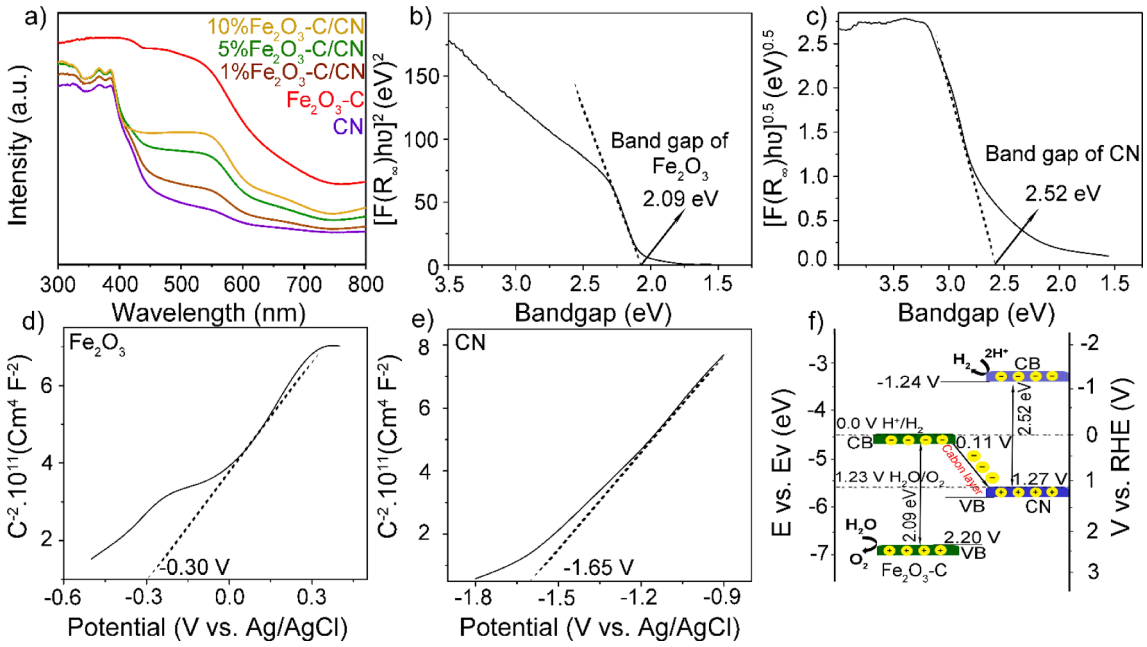

Fig. 4. A) uv–vis absorption spectra of pristine CN, Fe_2O_3-C, and Fe_2O_3-C/CN composites, b, c) Tauc plots of the UV–vis analysis by using Kubelka-Munk (KM) transformation of the pristine Fe_2O_3-C and CN, d, e) Mott-Schottky plots for Fe_2O_3-C and CN photocatalysts measured at 1.0 kHz in a Na_2SO_4 electrolyte and f) the electronic band structure of Fe_2O_3-C, and CN obtained from a collective analysis of bandgap energy.

were determined to be 2.20 and 1.27 eV, respectively, based on observations of M-S plots. To further the understanding of the energy band structure, UPS analysis was conducted to determine the work functions (Φ) and VBM of the as-fabricated samples using equations (S2-S6).

Fig. S4 (c) shows $E_{cut\text{-}off}$ for Fe_2O_3-C and CN were 16.26 and 17.24 eV, respectively. The electron work function (Φ) for Fe_2O_3-C and CN was estimated to be 4.96 and 3.98 eV, respectively using Equation (S2). The Fermi level (E_f), which is the negative value of Φ, was determined to be − 4.96 and −3.98 eV for Fe_2O_3-C and CN, respectively. The valence band top energy (E_{VB}) relative to the vacuum level was determined by adding the values of VB_{UPS} (the lower emission onset energy) with Φ, as indicated in Equation (S3). The VB_{UPS} spectra for Fe_2O_3-C and CN were produced by projecting the left slope to the baseline, resulting in values of 2.02 and 2.13 eV, respectively Fig. S4 d. Thus, the estimated E_{VB} was −7.054 eV for Fe_2O_3-C and −6.123 eV for CN. The values of E_{VB} and E_f for Fe_2O_3-C were determined as +2.20 and + 0.18 V (E, vs. NHE, pH = 7) using the conversion formula (S4) and Nernst equation (S5). On the other hand, values of E_{VB} and E_f for CN were determined as +1.27 and −0.86 V (E, vs. NHE, pH = 7). As a result, the CB potentials (E_{CB}) for Fe_2O_3-C and CN were determined to be 0.11 and −1.25 V (E, versus NHE, pH = 7) respectively, using Eq. (S7). The comprehensive calculation is provided in the supplementary information. Fig. S4 e) depicts the band structures of Fe_2O_3-C and CN before and after the creation of the connection, as inferred from the observations. The primary factor that drives charge transportation in heterojunction nanocomposites is the fluctuation in Φ or E_f for semiconductor photocatalysts. Fe_2O_3-C exhibits a higher work function (Φ) of 4.96 eV and a lower Fermi energy (E_f) of −4.96 eV, while CN has a lower work function (Φ) of 3.98 eV and a higher E_f of −3.98 eV (Fig. S4 e i). In addition, the formation of heterojunction results in the rapid movement of electrons from Fe_2O_3-C to CN through the conductive carbon layer until the equilibrium E_f is reached (Fig. S4 ii). The photo-generated electrons in the conduction band of Fe_2O_3-C are effectively transferred to the valence band of CN through the conductive carbon layer. They then recombine with the holes generated in the VB of CN (Fig. S4 iii). The charge transfer behavior of this heterojunction corresponds to the XPS data and is in line with the Z-scheme mechanism. As a result, the electrons in the conduction band of CN and the holes produced in the valence band of Fe_2O_3-C are retained. These retained electrons and holes play a role in the photocatalytic redox reactions, as shown in Fig S4 e iii) (Qaraah et al., 2023, 2022).

Based on the above calculation and the band alignment the proposed mechanism can also be drawn and shown in Fig. 4f. Furthermore, additional electrochemical impedance spectroscopy (EIS) measurements at multiple frequencies (i.e. 1000 Hz, 1500 Hz, and 2000 Hz), respectively were conducted as shown in Fig. S5 to obtain a more comprehensive dataset. This will allow us to accurately determine the flat band potential of Fe_2O_3-C and CN. After careful observation, we concluded that the flat band potential values of Fe_2O_3-C and CN are 0.30, and −1.65 eV respectively which are consistent with our previous findings.

3.4. Mechanism analysis

Fig. 5 shows the photocatalytic behavior of pure water splitting of the optimized composite (5 wt% Fe_2O_3-C/CN) composites along with their mass activity under solar irradiation (λ ≥ 420 nm) without using any sacrificial agent. The optimized heterostructure demonstrates an efficient Z-scheme mechanism for pure water splitting, with a conductive carbon layer acting as a crucial mediator between Fe_2O_3 and CN. Upon light irradiation, both Fe_2O_3 and CN absorb visible light, generating electron-hole pairs. The carbon layer facilitates the transfer of electrons from the conduction band (CB) of Fe_2O_3 to the valence band (VB) of CN, effectively reducing the recombination rate of photogenerated charge carriers due to its excellent conductivity. This conductive pathway provided by the carbon layer enhances charge mobility and spatially separates electron-hole pairs, thereby increasing the overall photocatalytic efficiency. Additionally, the carbon layer increases the surface area and offers additional active sites for photocatalytic reactions, further improving efficiency. In this Z-scheme mechanism, electrons in the CB of CN reduce water to produce hydrogen gas (H_2), while holes in the VB of Fe_2O_3 oxidize water to produce oxygen gas (O_2). The integration of Fe_2O_3 and CN through the carbon layer enhances photocatalytic performance by ensuring efficient charge transfer, protecting Fe_2O_3 from photo-corrosion, and synergistically increasing the photocatalytic activity compared to individual components. Thus, the Fe_2O_3-C/CN heterostructure, facilitated by the carbon

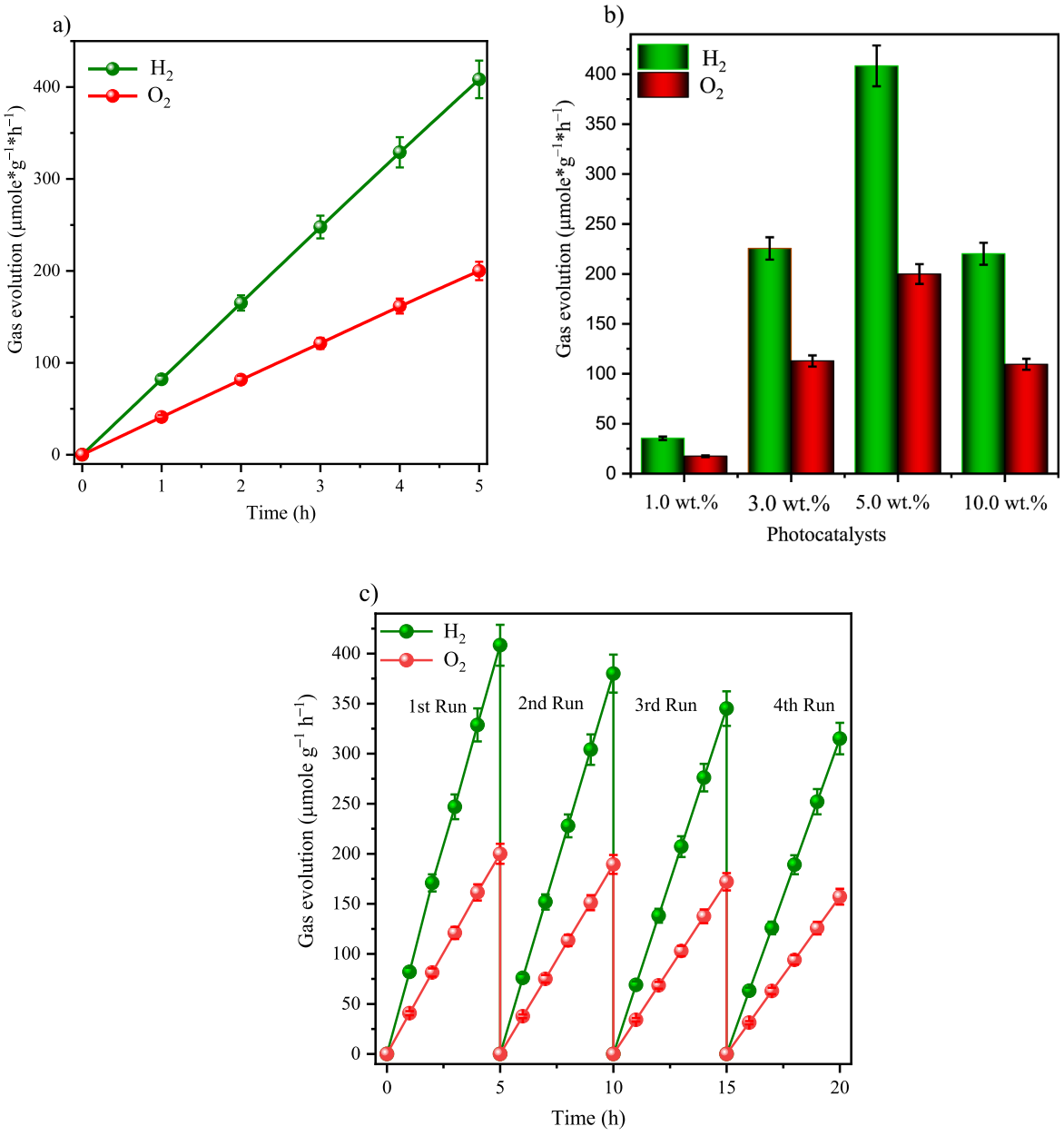

Fig. 5. A) hydrogen and oxygen evolution rate at 5 wt% of Fe_2O_3-C/CN photocatalyst during pure water splitting under visible light illumination, b) the corresponding mass activity, and c) photocatalytic stability of the 5 wt% of Fe_2O_3-C/CN as tested for 20 h with an evacuation at 5 h intervals.

layer, is a promising candidate for sustainable hydrogen production through solar-driven water splitting. The photocatalytic activity increased significantly at an optimum Fe_2O_3-C concentration (i.e. 5 wt %.) where the rate of hydrogen and oxygen evolution reaches up to 408 and 199 μmol*g^{-1}*h^{-1} (i.e. 2:1), respectively. The efficiency of converting solar-to-hydrogen energy reaches 0.29 % when utilizing an AM 1.5 G filter using the S1 equation. Usually, pristine CN and Fe_2O_3 have no potential for pure water splitting because of the high recombination rate whereas in the case of Fe_2O_3 the conduction band is more positive and it is not suitable for pure water splitting. As shown in Fig. S6 and for comparison, the photocatalytic activity of the optimized (5 wt% Fe_2O_3/CN) composite was found to be significantly lower than that of the optimized (5 wt% Fe_2O_3-C/CN) composite. The obtained results were also compared to those of other CN-based heterostructures including Fe_2O_3, as shown in Table S2 of the Supporting Information. From Table S2 it is evident that our Fe_2O_3-C/CN composite demonstrates superior photocatalytic performance in terms of pure water splitting compared to other state-of-the-art photocatalysts. The hydrogen/oxygen evolution rate of 499/199 μmol·g^{-1}·h^{-1} is among the highest reported, indicating the effectiveness of our material in photocatalytic water splitting.

The highest activity observed for 5 wt% Fe_2O_3-C/CN, can be attributed to the heterojunction following the Z-scheme mechanism (Fig. 4f) that suppresses the recombination process through the conductive carbon layer and enhances the photocatalytic activity. A Z-scheme band alignment (Fig. 4f) could be formed for the heterostructure, where the CB and VB of CN lie at −1.24 and 1.27 eV, corresponding to Fe_2O_3-C located at 0.11 and 2.20 eV, respectively. It is worth pointing out that the positive CB potential excluded the possibility of hydrogen generation from Fe_2O_3. This idea suggests that hydrogen evolves from the CB of CN. Simply we can say that the photogenerated electrons at the CB from Fe_2O_3 will be consumed by the holes generated at VB of CN through a conductive carbon layer following a Z-scheme mechanism and suppresses the recombination process. On the other hand, electrons in the

CB of CN react with water molecules to generate H^+ which is further converted to H_2, while the holes generated in the VB of Fe_2O_3-C can oxide the water molecules to generate O_2.

To confirm the Z-scheme mechanism of the Fe_2O_3-C/CN heterostructure, we performed Electron Paramagnetic Resonance (EPR) analysis. EPR is a powerful tool for detecting and characterizing paramagnetic species, including unpaired electrons and reactive oxygen species, which are crucial for understanding the charge transfer processes in photocatalytic systems. No signals of DMPO- •OH, and $•O_2^-$ were found in the absence of light as shown in Fig. S7 a, c. The EPR spectra of the optimized composite (5 wt% Fe_2O_3-C/CN) reveal the presence of hydroxyl radicals (•OH) under visible light irradiation as shown in Fig. S7 b. The •OH radicals are detected by their characteristic quartet signal in the presence of the spin-trapping agent DMPO. The formation of •OH radicals indicates that photoexcited holes in the valence band (VB) of Fe_2O_3-C are involved in the oxidation of water molecules, producing •OH radicals. Similarly, the EPR spectra of the Fe_2O_3-C/CN composite show a characteristic signal corresponding to superoxide radicals ($•O_2^-$) under visible light irradiation as shown in Fig. S7 d. This indicates the generation of $•O_2^-$ radicals in the composite, suggesting efficient charge separation and transfer. The EPR analysis provides direct evidence for forming both superoxide ($•O_2^-$) and hydroxyl (•OH) radicals, confirming the Z-scheme charge transfer mechanism in the Fe_2O_3-C/CN heterostructure. The observed EPR signals under visible light irradiation demonstrate that the photoexcited electrons in the CB of CN effectively participate in the reduction process, while holes in the VB of Fe_2O_3-C actively participate in the oxidation process. This charge transfer pathway is consistent with the Z-scheme mechanism, where the spatial separation of charge carriers reduces recombination and enhances photocatalytic efficiency (Xu et al., 2024; Zhang et al., 2024b).

Platinum (Pt) is widely recognized as an effective cocatalyst in photocatalysis due to its exceptional ability to facilitate charge separation and provide active sites for hydrogen evolution reactions (HER). Optimizing the Pt content is crucial for maximizing the photocatalytic activity of the samples, as it directly influences the efficiency of electron capture, hydrogen production, and overall stability of the photocatalyst. Pt provides numerous active sites for the HER, facilitating the reduction of protons to hydrogen gas. The high catalytic activity of Pt for HER is due to its optimal hydrogen adsorption energy, which ensures rapid and efficient hydrogen evolution (Tsao et al., 2021). To further confirm the suggested mechanism, here we also conducted an additional experiment involving the photo-deposition of Pt onto the surface of the optimized composite photocatalyst (5 wt% Fe_2O_3-C/CN). In this scenario, Pt nanoparticles will deposit in situ at sites where their high-valence counterpart is reduced. As shown in Fig. 6, the STEM mapping image of the Fe_2O_3-C/CN heterostructure revealed the deposition of Pt deposit generally located at the surface of CN, verifying the reduction place over the Fe_2O_3-C/CN heterostructure. The direct Z-scheme proposed mechanism of the Fe_2O_3-C/CN heterojunction photocatalyst is demonstrated in Fig. 4f. Despite the absence of a carbon layer, the redox potentials of the composite photocatalyst have been effectively maintained through the utilization of this Z-scheme pathway, the relatively slow charge transfer at the interface of Fe_2O_3 and CN still leads to severe recombination of the charge carriers at each component. As a result, photocatalytic pure water splitting over 5 wt% Fe_2O_3-C/CN was promoted at a limited level. Due to this reason, we believe that the formation of the conductive carbon layer on the surface of Fe_2O_3 plays a critical role in the acceleration of interfacial charge transfer, suppresses the recombination process, and enhances the activity of pure water splitting.

The photocatalyst stability is crucial for practical applications, therefore, the optimized photocatalyst composition of 5 wt% of Fe_2O_3-

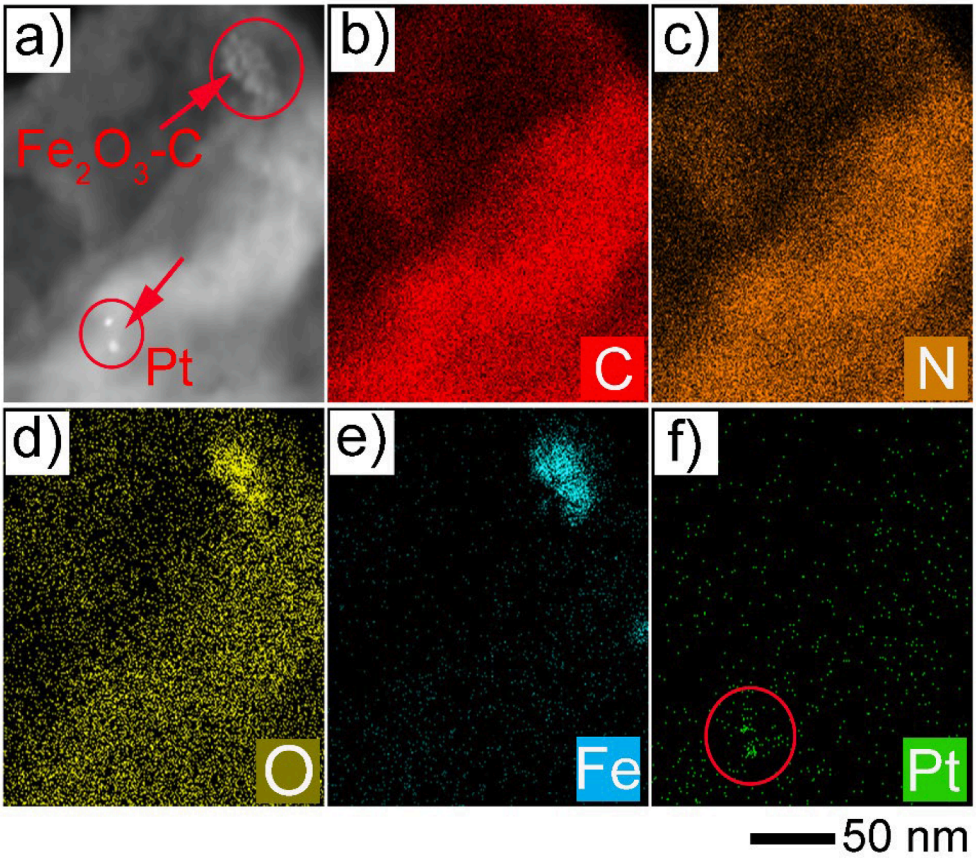

Fig. 6. A) stem image of fe_2O_3-C/CN heterostructure with deposited Pt nanoparticles, and b-f) the corresponding elemental mapping analysis of C, N, O, Fe, and Pt deposition on the composite, respectively.

C/CN was tested for pure water splitting for a period of 20 h with an evacuation at 5 h intervals as shown in Fig. 5c. The hydrogen and oxygen evolution rates were retained which shows excellent stability. After the photocatalytic reaction, the composite photocatalyst was characterized by XRD, FTIR, and TEM analyses (see Figs. S8). These outcomes also determine the excellent stability of the composite photocatalyst (Fe_2O_3-C/CN). Finally, the activity of the remaining composite photocatalysts is shown in Fig. S9.

3.5. Optical analysis

To study the charge transfer, separation, superiority of conductive carbon layer, and carrier efficiency mechanism of the photo-generated e^-/h^+ pairs in pristine CN and optimized composite a photo-luminescence (PL) analysis was carried out at room temperature as shown in Fig. 7a. The PL spectra of pristine CN, and the 5 wt% Fe_2O_3-C/CN composite was obtained at an excitation wavelength of 337 nm. As depicted in Fig. 7a, the peak intensity of the optimized composite (5 wt.%Fe_2O_3-C/CN) quenched as compared to the pristine CN, representing the supportive role of the conductive carbon layer (C) in suppressing the recombination process and enhancing the lifetime of photoexcited charge carriers. Notably the optimized composite of 5 wt% Fe_2O_3-C/CN exhibits the weakest peak intensity, being consistent with the pure water splitting results. It also implies intimate interfacial contact between Fe_2O_3-C and CN, which forms the basis for achieving rapid interfacial charge transfer. Furthermore, an electrochemical impedance spectroscope (EIS) was carried out to examine the behavior of charge transfer and resistance in the composite during interfacial charge transfer as shown in Fig. 7b. In comparison to pristine CN and Fe_2O_3-C, the optimized composite (5 wt% Fe_2O_3-C/CN) exhibits a substantially smaller arc radius in EIS Nyquist plot, indicating significantly lower charge transfer resistance. Thus, it is hypothesized that the conductive carbon layer enhances the charge transfer behavior at the interface between CN and Fe_2O_3-C photocatalytic materials. This understanding was further confirmed via Transient photocurrent response and linear sweep voltage (LSV) measurements of the pristine CN, Fe_2O_3-C, and 5 wt% Fe_2O_3-C/CN photoelectrode in Na_2SO_4 electrolyte solution as shown in Fig. 8. Fig. 8a illustrates the photocurrent response curves of the pure CN, Fe_2O_3-C, and optimized composite photocatalysts when exposed to visible light in multiple cycles of intermittent illumination. Upon exposure to visible light, the photocatalyst experiences a progressive increase in photocurrent until it reaches a steady state. The experiment shows that the charge carriers generated in the photocatalyst were initially trapped by the surface trap state and then transferred to the deep trap state. When the light source is switched off, it is not possible to measure any photocurrent. The optimized composite photocatalyst demonstrates exceptionally elevated photoelectrochemical activity. This photocurrent increase confirms the conductive carbon layer enhances the interface connection and then promotes the electron transfer behavior which is also consistent with the order of pure water splitting activity. Finally, linear sweep voltage (LSV) analysis provides that optimized composite 5 wt% Fe_2O_3-C/CN is another evidence that shows a much-reduced overpotential and a significantly enhanced cathodic current density, suggesting a faster movement of electrons between CN and Fe_2O_3-C as shown in Fig. 8b. All these results demonstrate the vital role of the conductive carbon layer in facilitating a reliable path for fast charge transfer and reducing the electron-hole (e^-/h^+) pair recombination effect.

4. Conclusion

In summary, we effectively synthesized a heterojunction photocatalyst consisting of CN and Fe_2O_3-C heterostructure nanoparticles driven from MOF (MIL-235) pyrolysis. When exposed to visible light, the photocatalyst has been shown to significantly enhance pure water photo-splitting. The optimized composite heterojunction (5wt.%Fe_2O_3-C/CN) exhibited the maximum activity, i.e., simultaneous evolution of both hydrogen (408 μmol/g·h) and oxygen (199 μmol/·g·h). The efficiency of converting sola-to-hydrogen energy is as high as 0.29 %. We propose a direct Z-scheme photocatalytic mechanism that utilizes highly active photogenerated charge carriers to drive redox reactions. Remarkably, it had been demonstrated that the layer of carbon on the surface of Fe_2O_3 played a vital role in obtaining the high photocatalytic activity. To aid in the interfacial electron transfer process, the carbon layer at the interface between CN and Fe_2O_3 may act as an electron channel. Put another way, through this special carbon layer, photogenerated electrons in the CB of Fe_2O_3 could quickly move to the VB of CN, avoiding the individual recombination process. Additionally, a straightforward in-situ photo deposition technique using Pt as an index of the reduction active sites supported the reaction mechanism. Finally, this investigation provides other research ideas for numerous photocatalytic processes in addition to indicating a great deal of potential for using such a photocatalyst for solar water splitting.

CRediT authorship contribution statement

Muhammad Qasim: Writing – original draft, Validation, Methodology, Investigation, Formal analysis, Conceptualization. **Muhammad**

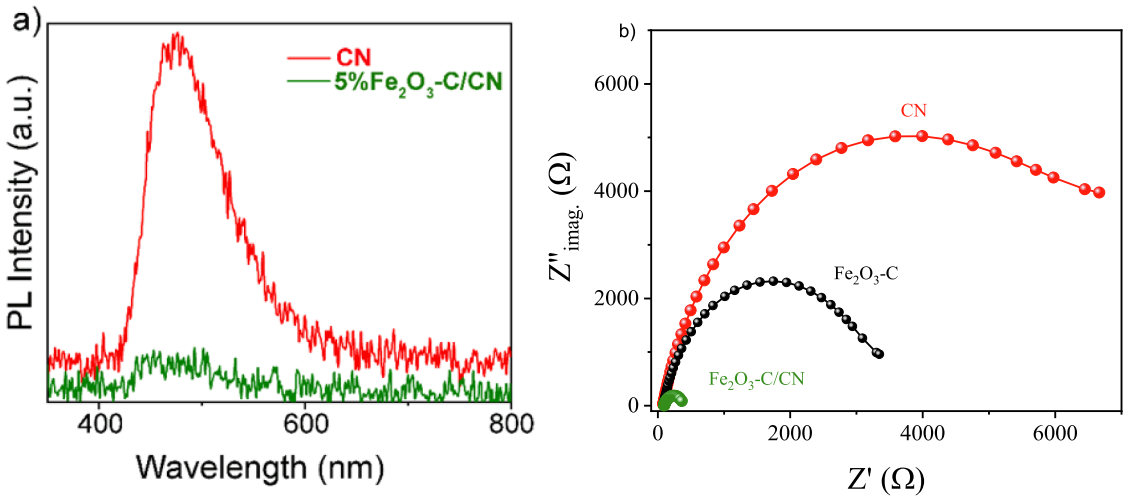

Fig. 7. A) pl analysis plots for cn and optimized composite fe_2O_3-C/CN and b) the corresponding Nyquist plots of electrochemical impedance spectroscopy in the dark obtained at a frequency ranging from 1 Hz to 10 kHz.

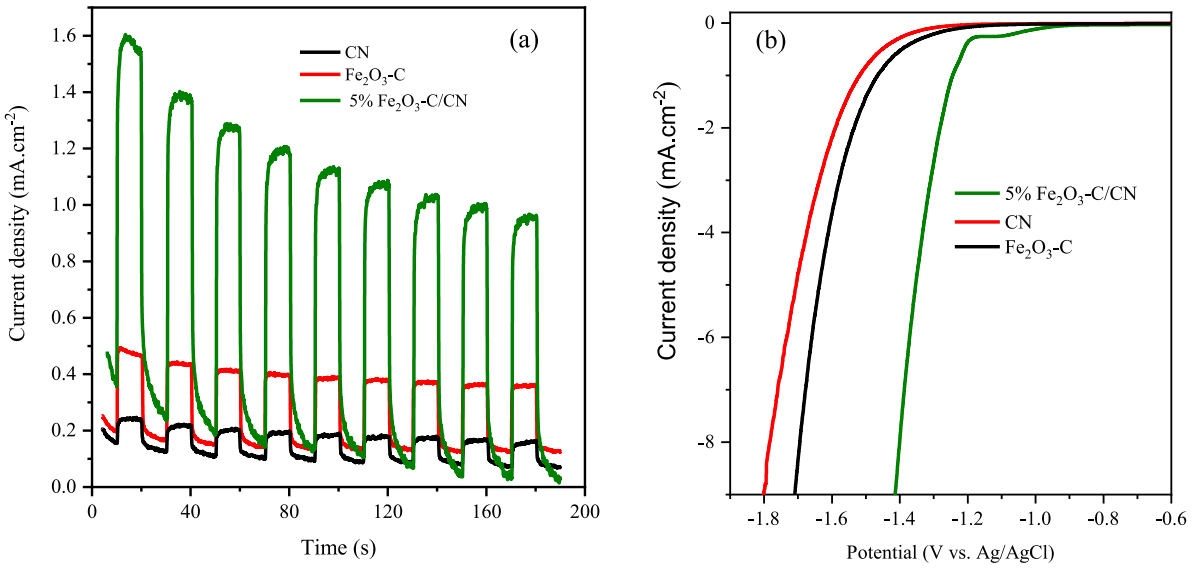

Fig. 8. A) transient photocurrent responses of fe_2O_3-C, CN, and an optimized composite of the as-prepared photocatalysts at a potential of 0.6 V (vs. Ag/AgCl) respectively, and b) LSV curves of pristine Fe_2O_3-C, CN, and optimized composite respectively.

A. Younis: Resources, Methodology, Data curation. **Fahim A. Qaraah:** Software, Resources, Investigation, Formal analysis. **Mohamed A. Ghanem:** Writing – review & editing, Funding acquisition, Conceptualization.

Declaration of Competing Interest

The authors declare that they have no known competing financial interests or personal relationships that could have appeared to influence the work reported in this paper.

Acknowledgements

This work was supported by the Qilu Institute of Technology, Zhangqiu Jinan China.

The authors would also like to express their sincere gratitude to the Researchers Supporting Program, Project number (RSP2024R518), King Saud University, Riyadh, Saudi Arabia.

Appendix A. Supplementary material

Supplementary data to this article can be found online at https://doi.org/10.1016/j.arabjc.2024.105902.

References

Ayodhya, D., 2023. Semiconductors-based Z-scheme materials for photoelectrochemical water splitting: a review. Electrochim Acta 448. https://doi.org/10.1016/j.electacta.2023.142118.

Bi, F., Ma, S., Gao, B., Yang, Y., Wang, L., Fei, F., Xu, J., Huang, Y., Wu, M., Zhang, X., 2023a. Non-oxide supported Pt-metal-group catalysts for efficiently CO and toluene co-oxidation: difference in water resistance and degradation intermediates. Fuel 344. https://doi.org/10.1016/j.fuel.2023.128147.

Bi, F., Wei, J., Gao, B., Liu, N., Xu, J., Liu, B., Huang, Y., Zhang, X., 2023b. New insight into the antagonism mechanism between binary VOCs during their degradation over Pd/ZrO2 catalysts. ACS ES T Eng. https://doi.org/10.1021/acsestengg.3c00630.

Chen, Y.A., Wang, Y.T., Moon, H.S., Yong, K., Hsu, Y.J., 2021. Yolk-shell nanostructures: synthesis, photocatalysis and interfacial charge dynamics. RSC Adv. https://doi.org/10.1039/d1ra00803j.

Dang, V.D., Annadurai, T., Khedulkar, A.P., Lin, J.Y., Adorna, J., Yu, W.J., Pandit, B., Huynh, T.V., Doong, R.A., 2023. S-scheme N-doped carbon dots anchored g-C3N4/Fe2O3 shell/core composite for photoelectrocatalytic trimethoprim degradation and water splitting. Appl Catal B 320. https://doi.org/10.1016/j.apcatb.2022.121928.

Danish, M., Saud Athar, M., Ahmad, I., Warshagha, M.Z.A., Rasool, Z., Muneer, M., 2022. Highly efficient and stable Fe2O3/g-C3N4/GO nanocomposite with Z-scheme electron transfer pathway: Role of photocatalytic activity and adsorption isotherm of organic pollutants in wastewater. Appl Surf Sci 604. https://doi.org/10.1016/j.apsusc.2022.154604.

Das, S., Deka, T., Ningthoukhangjam, P., Chowdhury, A., Nair, R.G., 2022. A critical review on prospects and challenges of metal-oxide embedded g-C3N4-based direct Z-scheme photocatalysts for water splitting and environmental remediation. Appl. Surface Sci. Adv. 11 https://doi.org/10.1016/j.apsadv.2022.100273.

Du, F., Lai, Z., Tang, H., Wang, H., Zhao, C., 2023. Construction of dual Z-scheme Bi2WO6/g-C3N4/black phosphorus quantum dots composites for effective bisphenol A degradation. J Environ Sci (china) 124. https://doi.org/10.1016/j.jes.2021.10.027.

Gong, Q., Zhou, Y., Wang, R., Jiao, W., 2022. Enhanced photocatalytic pure water splitting of porous g-C3N4/CdS composite by the bimetallic phosphide. J Environ Chem Eng 10. https://doi.org/10.1016/j.jece.2022.108046.

Gui, Y., Liu, Z., Feng, X., Jia, Y., Zhang, Y., Zhang, Y., Shi, J., 2024. One-step electrodeposition synthesis of NiFePS on carbon cloth as self-supported electrodes for electrochemical overall water splitting. J. Colloid Interf. Sci. 673 https://doi.org/10.1016/j.jcis.2024.06.096.

Hou, F., Lu, K., Liu, F., Xue, F., Liu, M., 2022. Manipulating a TiO2-graphene-Ta3N5 heterojunction for efficient Z-scheme photocatalytic pure water splitting. Mater Res Bull 150. https://doi.org/10.1016/j.materresbull.2022.111782.

Hussein Abdurahman, M., Zuhairi Abdullah, A., Da Oh, W., Fazliani Shopware, N., Faisal Gasim, M., Okoye, P., Ul-Hamid, A., Rahman Mohamed, A., 2023. Tunable band structure of synthesized carbon dots modified graphitic carbon nitride/bismuth oxychlorobromide heterojunction for photocatalytic degradation of tetracycline in water. J. Colloid Interface Sci. 629 https://doi.org/10.1016/j.jcis.2022.08.172.

Iqbal, S., Liu, J., Ma, H., Liu, W., Zuo, S., Yu, Y., Khan, A., 2023. Development of TiO2 decorated Fe2O3QDs/g-C3N4 Ternary Z-scheme photocatalyst involving the investigation of phase analysis via strain mapping and its photocatalytic performance under visible light illumination. Res. Chem. Intermed. 49 https://doi.org/10.1007/s11164-023-04987-8.

Ji, R., Wang, L., Wu, H., Meng, F., Jin, H., Han, D., Liu, Y., 2024. A nickel-based dendritic electrode matrix with high surface efficiency mass transfer for highly efficient overall water splitting. J. Clean. Prod. 460 https://doi.org/10.1016/j.jclepro.2024.142631.

Jiang, L., Yuan, X., Zeng, G., Liang, J., Wu, Z., Wang, H., 2018. Construction of an all-solid-state Z-scheme photocatalyst based on graphite carbon nitride and its enhancement to catalytic activity. Environ. Sci Nano. https://doi.org/10.1039/c7en01031a.

Kumar, S.S., Lim, H., 2023. Recent advances in hydrogen production through proton exchange membrane water electrolysis - a review. Sustain. Energy Fuels. https://doi.org/10.1039/d3se00336a.

Ma, X., Liu, X., Zhang, X., Piao, C., Liu, Z., Fang, D., Wang, J., 2021. Construction of dual Z-scheme NiO/NiFe2O4/Fe2O3 photocatalyst via incomplete solid state chemical combustion reactions for organic pollutant degradation with simultaneous hydrogen production. Int. J. Hydrogen Energy 46. https://doi.org/10.1016/j.ijhydene.2021.07.076.

Ma, H., Luo, Q., Zhou, J., Reddy, N., Wang, H., Zhang, Y., 2023. Synthesis of photosensitive catalysts with wide-band absorption and ability to enhance the degradation of polyester fabric wastes. Chem. Eng. J. 454 https://doi.org/10.1016/j.cej.2022.140377.

Ma, S., Zhou, Z., Zhang, Y., Rao, R., Han, H., Liang, J., Zhao, Z., Bi, F., Liu, N., Zhang, X., 2024. Review of irradiation treatments on MOFs and COFs: synthesis, modification,

and application. Sep. Purif. Technol. https://doi.org/10.1016/j.seppur.2024.126636.
Palanivel, B., Hossain, M.S., Raghu, M.S., Kumar, K.Y., Macadangdang, R.R., Ubaidullah, M., Prakash, C., Bommireddy, P.R., Park, S.H., 2023. Green synthesis of Fe2O3 deposited g-C3N4: addition of rGO promoted Z-scheme ternary heterojunction for efficient photocatalytic degradation and H2 evolution reaction. Mater. Res. Bull 162. https://doi.org/10.1016/j.materresbull.2023.112177.
Pang, H., Zhou, W., Hu, H., Liu, L., Ye, J., Wang, D., 2023. Polar-surface-dominated zigzag GaN nanowires with alternate H2 and O2 evolution sites for photocatalytic overall water splitting. Appl. Catal. A Gen. 654 https://doi.org/10.1016/j.apcata.2023.119084.
Qaraah, F.A., Mahyoub, S.A., Hezam, A., Qaraah, A., Xin, F., Xiu, G., 2022. Synergistic effect of hierarchical structure and S-scheme heterojunction over O-doped g-C_3N_4/N-doped Nb_2O_5 for highly efficient photocatalytic CO_2 reduction. Appl. Catal. B 315. https://doi.org/10.1016/j.apcatb.2022.121585.
Qaraah, F.A., Mahyoub, S.A., Drmosh, Q.A., Qaraah, A., Xin, F., 2023. One-step fabrication of unique 3D/2D S, O-doped g-C_3N_4 S-scheme isotype heterojunction for boosting CO_2 photoreduction. Mater. Today Sustain. 23 https://doi.org/10.1016/j.mtsust.2023.100437.
Qasim, M., Xue, F., Liu, M., Guo, L., 2019. Phase-transition-induced one-dimensional amorphous α-Fe2O3/β-FeOOH homojunction for efficient photocatalytic water oxidation. J. Photon. Energy 9. https://doi.org/10.1117/1.jpe.9.026501.
Qasim, M., Liu, M., Guo, L., 2021. Electron transfer via a carbon channel for efficient Z-scheme solar hydrogen production. Int. J. Hydrogen Energy 46. https://doi.org/10.1016/j.ijhydene.2021.06.074.
Qasim, M., Liu, M., Guo, L., 2023. Z-scheme P-doped-g-C3N4/Fe2P/red-P ternary composite enables efficient two-electron photocatalytic pure water splitting. Catal. Today 409. https://doi.org/10.1016/j.cattod.2022.05.007.
Rao, R., Huang, Y., Ling, Q., Hu, C., Dong, X., Xiang, J., Zhou, Q., Fang, S., Hu, Y., Zhang, Y., Tang, Q., 2023. A facile pyrolysis synthesis of Ni doped Ce2O3@CeO2/CN composites for adsorption removal of Congo red: activation of carbon nitride structure. Sep Purif Technol 305. https://doi.org/10.1016/j.seppur.2022.122505.
Sarkar, P., De, S., Neogi, S., 2022. Microwave assisted facile fabrication of dual Z-scheme g-C3N4/ZnFe2O4/Bi2S3 photocatalyst for peroxymonosulphate mediated degradation of 2,4,6-trichlorophenol: the mechanistic insights. Appl. Catal B 307. https://doi.org/10.1016/j.apcatb.2022.121165.
Sun, L., Yu, X., Tang, L., Wang, W., Liu, Q., 2023. Hollow dodecahedron K3PW12O40/CdS core-shell S-scheme heterojunction for photocatalytic synergistic H2 evolution and benzyl alcohol oxidation. Chin. J. Catal. 52 https://doi.org/10.1016/S1872-2067(23)64507-3.
Tsao, C.-W., Fang, M.-J., Hsu, Y.-J., 2021. Modulation of interfacial charge dynamics of semiconductor heterostructures for advanced photocatalytic applications coordination. Chem. Rev. 438 (2021), 213876.
Vignesh, S., Suganthi, S., Srinivasan, M., Tamilmani, A., Sundar, J.K., Gedi, S., Palanivel, B., Shaikh, S.F., Ubaidullah, M., Raza, M.K., 2022. Investigation of heterojunction between α-Fe2O3/V2O5 and g-C3N4 ternary nanocomposites for upgraded photo-degradation performance of mixed pollutants: efficient dual Z-scheme mechanism. J. Alloys Compd. 902 https://doi.org/10.1016/j.jallcom.2022.163705.
Wang, W., Mei, S., Jiang, H., Wang, L., Tang, H., Liu, Q., 2023. Recent advances in TiO_2-based S-scheme heterojunction photocatalysts. Chin. J. Catal. https://doi.org/10.1016/S1872-2067(23)64551-6.
Wei, J., Zhang, Y., Zhou, Z., Bi, F., Qiao, R., Jiang, S., Wang, J., Zhang, X., 2023a. PVP-modified spindle-shaped MIL-88B(Fe) to enhance the degradation of tetracycline by activated peroxodisulfate: a comparative study and mechanistic investigation. Prog. Nat. Sci.: Mater. Int. 33 https://doi.org/10.1016/j.pnsc.2023.12.020.
Wei, Y., Zhang, Z., Wang, W., Song, Z., Cai, M., Sun, S., 2023b. Photocatalytic Z-scheme overall water splitting: insight into different optimization strategies for powder suspension and particulate sheet systems. ChemPhysChem. https://doi.org/10.1002/cphc.202300216.
Xiao, M., Jiao, Y., Luo, B., Wang, S., Chen, P., Lyu, M., Du, A., Wang, L., 2023. Understanding the roles of carbon in carbon/g-C3N4 based photocatalysts for H2 evolution. Nano Res 16. https://doi.org/10.1007/s12274-021-3897-7.
Xu, M., Yu, F., Liu, Y., Li, W., Li, C., Song, F., Qiu, J., 2024. Integrating uranyl-affinity "hooks" into conjugated polymers achieving giant built-in electric field for boosting photocatalytic uranium extraction from seawater. Macromolecules. https://doi.org/10.1021/acs.macromol.4c00717.
Xue, F., Si, Y., Wang, M., Liu, M., Guo, L., 2019. Toward efficient photocatalytic pure water splitting for simultaneous H2 and H2O2 production. Nano Energy 62. https://doi.org/10.1016/j.nanoen.2019.05.086.
Yavuz, C., Erten-Ela, S., 2022. Solar light-responsive α-Fe_2O_3/CdS/g-C_3N_4 ternary photocatalyst for photocatalytic hydrogen production and photodegradation of methylene blue. J Alloys Compd 908. https://doi.org/10.1016/j.jallcom.2022.164584.
Yu, X., Su, H., Zou, J., Liu, Q., Wang, L., Tang, H., 2022. Doping-induced metal–N active sites and bandgap engineering in graphitic carbon nitride for enhancing photocatalytic H2 evolution performance. Chin. J. Catal. 43 https://doi.org/10.1016/S1872-2067(21)63849-4.
Zeng, Y., Zhan, X., Hong, B., Xia, Y., Ding, Y., Cai, T., Yin, K., Wang, X., Yang, L., Luo, S., 2023. Surface atom rearrangement on carbon nitride for enhanced photocatalysis degradation of antibiotics under visible light. Chem. Eng. J. 452 https://doi.org/10.1016/j.cej.2022.139434.
Zhang, L., Jiang, S., Jia, Y., Zhang, M., Guo, J., 2024a. Effects of Na^+/H_2O_2 on nitrogen removal and sludge activity: performance and mechanism. J. Environ. Chem. Eng. 12 https://doi.org/10.1016/j.jece.2024.113194.
Zhang, X., Gao, B., Rao, R., Bi, F., Li, C., Yue, K., Wang, Y., Xu, J., Feng, X., Yang, Y., 2024b. Defects materials of Institut Lavoisier-125(Ti) materials enhanced photocatalytic activity for toluene and chlorobenzene mixtures degradation: Mechanism study. J Colloid Interface Sci 660. https://doi.org/10.1016/j.jcis.2024.01.012.
Zhang, H., Tian, W., Zhang, J., Duan, X., Liu, S., Sun, H., Wang, S., 2022. Carbon nitride-based Z-scheme photocatalysts for non-sacrificial overall water splitting. Mater Today Energy. https://doi.org/10.1016/j.mtener.2021.100915.
Zhao, D., Wang, Y., Dong, C.L., Huang, Y.C., Chen, J., Xue, F., Shen, S., Guo, L., 2021. Boron-doped nitrogen-deficient carbon nitride-based Z-scheme heterostructures for photocatalytic overall water splitting. Nat Energy 6. https://doi.org/10.1038/s41560-021-00795-9.
Zhou, X., Liu, H., Liu, S., zhang, L., Wang, T., Wang, C., Su, D., 2023. Constructing efficient α-Fe2O3/g-C3N4/HNTs-loaded heterojunction photocatalysts for photocatalytic oxidative desulfurization: Influencing factors, kinetics, and mechanism. Fuel 332. doi: 10.1016/j.fuel.2022.126147.